

# MOF-Derived Core-Shell La(OH)<sub>3</sub>@Cu(OH)<sub>2</sub>/Co(OH)<sub>2</sub> Heterostructure for Supercapacitors

Diab Khalafallah,<sup>\*[a, b]</sup> Yunxiang Zhang,<sup>[a]</sup> and Qinfang Zhang<sup>\*[a]</sup>

Structural metal-organic framework (MOF)-based pseudocapacitive components have exhibited significant potential for supercapacitors. Herein, a highly functioning vertically aligned La(OH)<sub>3</sub>@Cu(OH)<sub>2</sub>/Co(OH)<sub>2</sub> core-shell composite was *in situ* yielded from the template Co MOF-74 frameworks on the nickel foam (Co MOF/NF) via a dual approach of heterointerfacing and structural engineering. The sacrificial template Co MOF/NF microrods were converted into binary hydroxide Cu(OH)<sub>2</sub>/Co(OH)<sub>2</sub>/NF (Cu/Co/NF) junction with spatial nanogranule self-assembled microrods-like structure through a cation exchange reaction. Subsequently, the binary hydroxide Cu/Co junction was employed as a backbone to stabilize La(OH)<sub>3</sub> species via an electrodeposition process, forming a heterostructural La-

(OH)<sub>3</sub>@Cu/Co/NF (La@Cu/Co/NF) core-shell composite. Preliminary electrochemical analysis demonstrates the efficiency of the binder-free La@Cu/Co/NF core-shell electrode, revealing a specific capacitance value of 874.8 F g<sup>-1</sup> at 1 A g<sup>-1</sup> and high rate ability (65.2% capacitance retention at 30 A g<sup>-1</sup>). Hence, it combines rich electrochemical reactive sites for Faradaic redox reactions and the favorable synergistic effect of integrated constituents. The configured La@Cu/Co/NF//AC asymmetric supercapacitor (ASC) device boasts a maximum voltage window of 1.55 V, acquiring an energy density of 43.9 Wh kg<sup>-1</sup> at 775 W kg<sup>-1</sup>. Besides, the device maintains a capacitance retention rate of 76.4% even after enduring 11,000 charge-discharge cycles, suggesting good long-term durability.

## 1. Introduction

The demand for low-cost, high-performance, and sustainable electrochemical energy conversion and storage approaches has skyrocketed owing to fast advances in environment-friendly and renewable energy resources (e.g., hydropower, light, and wind).<sup>[1,2]</sup> The landmark exploration and utilization of novel electrochemical energy storage devices such as lithium-ion batteries, metal-ion batteries, supercapacitors, and so forth has inspired widespread implications in portable and wearable electronics, smart gadgets, hybrid vehicles, and digital telecommunication systems.<sup>[3-7]</sup> Recently, pseudocapacitors with reversible Faradaic redox reactions have presented as a leading choice in the seeking for efficient energy storage options due to their high capability to deliver energy at a fast rate, tunable power densities, cost-efficiency, extended cycling lifespans, and environmentally sustainable features.<sup>[8,9]</sup>

Generally speaking, the choice of an electrode material significantly affects the energy density of a supercapacitor device. Engineering the chemical composition of an electrode material can manipulate the redox properties, number of available oxidation states, and material's capability to participate in Faradaic reaction processes. Tailoring the composition offers opportunities to achieve favorable surface chemistries and porous structures, tune the electronic conductivity, increase

the effective utilization of active sites, and realize robust synergistic effects, which regulate the electrochemical performance, such as high capacitance, exceptional stability, and superior energy density.<sup>[10,11]</sup> Reactive compounds with high theoretical capacitance, large surface area, favorable porosities, tunable surface chemistry, and good conductivity can reveal greater energy densities, supporting the development of high-efficiency and powerful sustainable electrochemical energy storage devices. Pseudo-active and Faradaic materials (e.g., transition metal hydroxides/oxides, chalcogenides, phosphides, nitrides, and borides) with high electrochemical activity and versatile valence states facilitate the reversible Faradaic redox reactions during charge-discharge processes, typically providing high specific capacitance values, storing numerous charges per unit mass, and yielding larger energy densities as compared to purely electric double-layer (capacitive) components (e.g., carbon-based materials).<sup>[12,13]</sup> Notably, MOF-derived faradaic electrode materials have been extensively utilized for supercapacitors and secondary batteries because of their highly ordered structures, tunable porosity, and adjustable chemical composition.<sup>[14,15]</sup> Pseudocapacitive compounds are capable of operating at wider voltage ranges without degrading, maximizing the energy density. This is particularly significant for constructing hybrid systems that integrate capacitor and battery-like charge storage behaviors.<sup>[16]</sup> The rapid kinetics associated with pseudocapacitive processes manifest efficient energy delivery without sacrificing the energy density. The transition between multiple valence states may tune the cycling stability, allowing consistent performance and energy density during continuous operation. In particular, MOF-based multi-transition metal hydroxides or heterostructures display many advantages including plenteous electrochemical active sites, large specific surface area, regulated electronic configuration,

[a] D. Khalafallah, Y. Zhang, Q. Zhang  
School of Materials Science and Engineering, Yancheng Institute of Technology, Yancheng 224051, P. R. China  
E-mail: diab\_khalaf@energy.aswu.edu.eg  
qfangzhang@gmail.com

[b] D. Khalafallah  
Mechanical Design and Materials Department, Faculty of Energy Engineering, Aswan University, P.O. Box 81521 Aswan, Egypt

and synergistic effects of integrated structural reactive components.<sup>[17,18]</sup> Multi-component heterostructure materials with abundant heterojunctions are exceptionally attractive and experiencing growing importance in various energy-related fields due to hetero-interfacial effect and synergistic effect.<sup>[1,2]</sup> Such systems bring several advantageous compositional/structural merits, and trigger charge redistribution at heterointerfaces, thereby establishing robust electronic interactions (electron effect) and promoting the overall charge storage performance.<sup>[19]</sup> Alongside, the distinctive interfaces can considerably reduce the ion diffusion distances and modify the reaction kinetics of electrodes. Electrode materials combining abundant active sites with various valence states create synergistic effects, which further regulate the electrochemical performance and energy density. The heterogeneous interface in multi-component heterostructures can noticeably intensify the number of redox-active sites and expedite the charge transportation rate across interfaces, strengthening the inherent electro-capacitive behavior.<sup>[20,21]</sup>

What's more, through *in situ* heterointerfacing synthesis tactics, the intrinsic reactivity of electrode material, active site accessibility, and chemical and structural stability can be regulated. Binder-free electrode design in which electrochemically active species are directly trapped into flexible and conductive scaffolding can reinforce the interfacial connections between active components and current collectors and further enhance the energy storage capacity.<sup>[22,23]</sup> Electrode materials with a large specific surface area give rise to more reactive sites for electrochemical reactions, implying greater charges during operations. Upon increasing the surface area, more electrolyte ions can interact with the electrode active material and faster charge-discharge kinetics occur.<sup>[14,15]</sup> Enlarged surface area leads to better pseudocapacitive behavior, in which Faradaic reaction processes yield extra charge storage beyond the electric double-layer capacitance.<sup>[6]</sup> A large surface area generally correlates with a high capacitance value, enabling ultimate energy storage potential. Enhanced porosities and rich ion diffusion channels innervate the ion accessibility to reactive sites, speed up the electrolyte penetration into inner skins, optimize both capacitive and Faradaic charge storage mechanisms, and ensure a wide contact area with electrolyte ions for charge storage.<sup>[24]</sup> Higher porosity means abundant reactive sites for the charge accumulation, directly boosting the capacitance. All of which are crucial for maximizing the energy density. A suitable porous architecture can accommodate the volume expansion/contraction, resulting in better structural stability and longevity of electrode active material. Thus, the energy density can be preserved over continuous operation conditions.<sup>[25]</sup> High ionic and electronic conductivity is essential for boosting the energy density of supercapacitor technologies. Electrode materials with improved electric conductivity and low internal resistance usually display faster electron transport during electrochemical reactions, hence enhancing the charge storage kinetics and contributing to increased energy density.<sup>[26,27]</sup> Conductive supports often present good electrochemical stability, resulting in longer-lasting performance. Stable materials can maintain energy density over prolonged

charging-discharging cycling. Good ionic conductivity at the electrode/electrolyte interface ensures rapid ion movement. The effectiveness of ions in reaching exposed reactive sites is crucial to acquiring a high energy density.

Accordingly, motivated by the above discussions, this work describes the engineering of a heterostructural ternary hydroxide La@Cu/Co core-shell composite *in situ* on a micro-porous NF skeleton through a solvothermal method, cation exchange reaction, and electrodeposition process. The self-sacrifice template Co MOF anchored on the NF surface was transformed into the binary hydroxide Cu/Co junction via a cation exchange reaction. This leads to the emergence of a one-dimensional (1D) core-shell heterostructure, resembling a sandwich cookie with the La(OH)<sub>3</sub> decorating the binary hydroxide Cu/Co junction. Such special array microstructures can effectively tune the charge transfer and ion diffusion dynamics. The casting approach ensures uniform distribution of reactive components and direct contact with the current collector without any adhesives. Consistent with the anticipated findings, the resultant La@Cu/Co core-shell hybrid showcases high pseudocapacitive performance in terms of specific capacitance and rate capability. Thus, opening up a new possibility to further develop MOF-derived compounds for electrochemical energy storage technology.

## Experimental Section

### Fabrication of 1 D Co MOF/NF

All chemicals and reagents were directly investigated without additional purification. The NF piece (20 mm×40 mm×0.3 mm) was successively immersed into dilute HCl solution, ethanol absolute, and deionized water (DI) under ultrasonic treatment, each for 15 min. After washing, the NF was dried at 60 °C in an electric oven. A simple solvothermal approach was adopted to *in situ* anchor the Co MOF-74 microrods on the NF surface. In a typical process, 0.52 g Co(NO<sub>3</sub>)<sub>2</sub>·6H<sub>2</sub>O and 0.134 g 2,5-dihydroxyterephthalic acid (C<sub>8</sub>H<sub>6</sub>O<sub>6</sub>, DHTA) were inserted into 40 mL mixed solution (10 mL ethanol, 10 mL DI, and 20 mL N, N-dimethylformamide "DMF") under continuous magnetic stirring till complete decomposition. The as-formed reaction solution was then loaded into a 60 mL autoclave reactor with a well-cleaned NF substrate and maintained at 120 °C for 24 h. After cooling down to room temperature, the harvested brick-red Co MOF/NF electrode was carefully washed with ethanol and DI repeatedly and dried overnight at 60 °C. The mass loading was ~2.27 mg cm<sup>-2</sup>.

### Fabrication of Binary Hydroxide Cu/Co Junction on the NF

To yield the binder-free binary hydroxide Cu/Co junction, a cation exchange reaction was employed under hydrothermal conditions. In such a procedure, the as-prepared Co MOF/NF was immersed into 40 mL mixed solution (DI/ethanol = 1:1, V/V) containing a completely decomposed copper (II) chloride dihydrate (CuCl<sub>2</sub>·2H<sub>2</sub>O, 15 mM). The whole system was subsequently heated up to 120 °C for 2 h in an electric oven. The obtained binary hydroxide Cu/Co/NF junction was washed with ultrapure water and ethanol several times and dried in an oven.

## Synthesis of Ternary Hydroxide La@Cu/Co Core-Shell Composite

The  $\text{La}(\text{OH})_3$  film-decorated binary hydroxide Cu/Co junction was attained by a facile electrodeposition technique. The  $\text{La}(\text{OH})_3$  electrolytic solution was prepared by dissolving lanthanum nitrate hexahydrate ( $\text{La}(\text{NO}_3)_3 \cdot 6\text{H}_2\text{O}$ , 2 mM) in 40 mL DI under continuous stirring for 10 min. The electrochemical deposition process was carried out at room temperature in a traditional three-electrode cell configuration containing a platinum (Pt) plate and  $\text{Hg}/\text{HgO}$  as the counter and reference electrodes, respectively. Meanwhile, the as-synthesized Cu/Co/NF system served as the working electrode. The electrodeposition method was accomplished at a constant potential of  $-1.0\text{ V}$  for 300 s. The resultant ternary hydroxide La@Cu/Co/NF core-shell composite was then taken out, rinsed with DI water and ethanol, and finally placed in an oven at  $60^\circ\text{C}$  overnight.

## Materials Characterization

The samples' crystallographic structure and phase purity were analyzed by X-ray diffraction (XRD) measurements employing the Philip X-ray diffractometer with the Cu  $\text{K}\alpha$  irradiation system. The chemical states of components and valences were detected by X-ray photoelectron spectroscopy (XPS) technique using a Thermo Scientific, Escalab 250 Xi X-ray photoelectron spectroscopy equipped with a monochromatic Al Ka source. The obtained microstructures and morphologies were recorded by scanning electron microscopy (SEM, JEOL JEM-6300F) and transmission electron microscope (TEM) combined with an energy-dispersive X-ray spectroscopy (EDS). The specific surface area and porous texture of samples were monitored by the  $\text{N}_2$  adsorption-desorption technique (Micromeritics ASAP 2460). The specific surface area was calculated by the Brunauer-Emmett-Teller (BET) method. The content of elements was measured by an inductively coupled plasma mass spectroscopy (ICP-MS: Agilent 7850, 1550 W Power, and  $1\text{ L min}^{-1}$  auxiliary flow).

## Electrochemical Measurements

Electrochemical properties and pseudocapacitive performance of as-designed electrodes were evaluated in a 3 M KOH aqueous electrolyte solution at room temperature using a CHI 660 E electrochemical workstation. Cyclic voltammetry (CV), galvanostatic charge/discharge (GCD), and electrochemical impedance spectroscopy (EIS) techniques were measured to monitor the electrochemical behavior. The conventional three-electrode system was established with a Pt plate (10 mm $\times$ 10 mm $\times$ 0.1 mm),  $\text{Hg}/\text{HgO}$ , and synthesized sample (10 mm $\times$ 10 mm $\times$ 0.3 mm) as the counter, reference, and working electrodes, respectively. The gravimetric capacitance ( $C$ ,  $\text{F g}^{-1}$ ) was assessed based on the discharge results of GCD profiles as follows:

$$C = \frac{I \times \Delta t}{m \times \Delta V} \quad (1)$$

where  $I$ ,  $m$ ,  $\Delta t$ , and  $\Delta V$  reflect the discharge current (A), active loading of electrode material (g), discharge time (s), and working voltage range (V), respectively. To further investigate the charge storage capability of binder-free ternary hydroxide La@Cu/Co core-shell electrode, an ASC cell was fabricated utilizing the heterostructural La@Cu/Co/NF as the cathode and benchmarking activated carbon (AC)-modified NF as the anode in a 3 M KOH electrolyte. The AC-immobilized NF (AC/NF) was achieved via a slurry-loading process in which the AC, acetylene black carbon and polyvinylidene fluoride were mixed with a mass ratio of 80:10:10 utilizing certain

drops of N-Methyl-2-pyrrolidone solvent to form a homogeneous ink. The as-attained slurry was anchored on a well-purified NF substrate (10 mm $\times$ 10 mm $\times$ 0.3 mm) and dried overnight at  $60^\circ\text{C}$  to acquire the AC/NF anode. Before assembling the cell system, the mass ratio of the anode to the cathode electrode was calculated according to the charge storage balance rule as follows:

$$Q^- = Q^+, \quad Q = C \times m \times \Delta V \quad (2)$$

$$\therefore \frac{m^-}{m^+} = \frac{C^+ \times \Delta V^+}{C^- \times \Delta V^-} \quad (3)$$

where  $m^-/m^+$ ,  $C^-/C^+$ , and  $\Delta V^-/\Delta V^+$  demonstrate the average masses (g), specific capacitances ( $\text{F g}^{-1}$ ), and working voltage windows (V), respectively of the anode and cathode active material. The specific energy ( $\text{Wh kg}^{-1}$ ) and power ( $\text{W kg}^{-1}$ ) density outcomes could be estimated using the following formulas (Equations (4) & (5)):

$$E = \frac{C \times \Delta V^2}{7.2} \quad (4)$$

$$P = \frac{E \times 3600}{\Delta t} \quad (5)$$

## Results and Discussions

The ternary hydroxide La@Cu/Co/NF core-shell heterostructure electrode was developed and constructed via solvothermal process, cation exchange reaction, and electrodeposition method (Figure 1). Co MOF microrods were *in situ* stabilized on the NF skeleton as a result of the coordination between the DHTA and  $\text{Co}^{2+}$  ions in the reaction solution. During mild solvothermal treatment, the well-dissolved metal salt could release  $\text{Co}^{2+}$  ions which subsequently interacted with the DHTA to create Co MOF (Equation (6)). The resulting Co MOF microrods were subjected to a cation exchange reaction under hydrothermal conditions to form the binary hydroxide Cu/Co junction, in which the DHTA species were replaced by the  $\text{OH}^-$  (Equation (7)). Such a cationic exchange process can be affected by the mobility and substitution of cations between the solid and liquid phases. The Co ions of the parent MOF material diffuse out into the solution and get solvated, and concurrently the Cu ions are introduced into the lattice through inward diffusion. The variation in the ion concentration between the solid phase and liquid phase guides the ion movement from regions with a high concentration to regions with a low concentration for attaining dynamic equilibrium. The hydrothermal conditions which involve a relatively high temperature ( $120^\circ\text{C}$ ) and pressure regulate the ion movement and reactivity as well as achieve a lower energy barrier for the cation exchange process.<sup>[28]</sup> The thermodynamic driving force for the cationic exchange under these conditions tends to diminish the Gibbs free energy of the reaction system.<sup>[29]</sup> The chemical potential (a measure of the free energy per building unit within the system) of Co ions in the solid phase and Cu ions in the liquid phase plays a vital role in the cation exchange process. Ions usually move from a high chemical potential region to a low chemical potential region. Our proposed hydrothermal

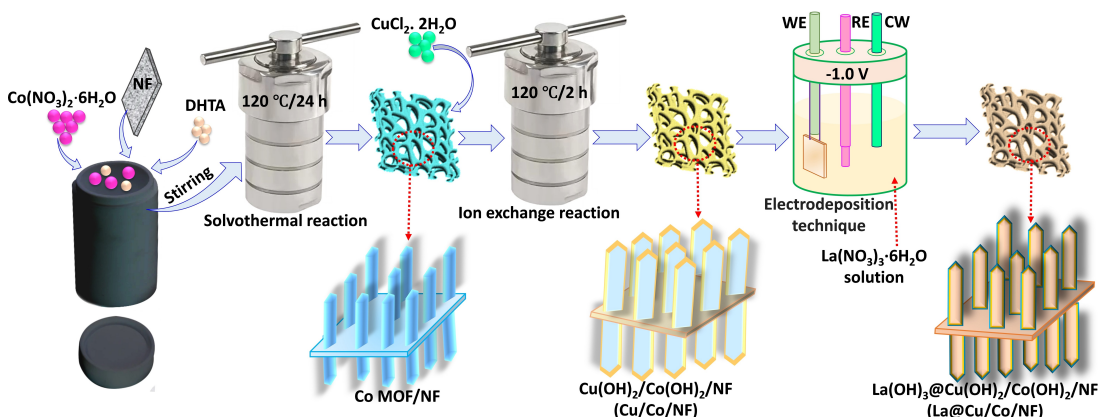
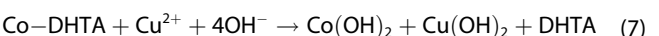


Figure 1. An illustrative scheme describing the design of a heterostructural ternary hydroxide La@Cu/Co/NF core-shell electrode.

conditions can alter the chemical potential of Co and Cu ions in both solid and liquid phases, respectively, enabling more soluble Co ions and certain Cu ions more likely to enter the solid phase. The Co and Cu ions will continue moving till their corresponding chemical potentials in both solid and liquid phases are similar, thus ensuring equilibrium. The diversity in the chemical potential between the solid and liquid phases represents the driving force for the cation exchange reaction.<sup>[30]</sup> The hydrothermal conditions may reduce the crystal lattice rigidity of the solid phase and create compatible ion sites, increasing its ability to accommodate Cu ions from the solution. Besides, the MOF platform with lower lattice energy (which stems from interactions between organic ligand and metal centers) permits flexibility in hosting ions of various charges and sizes, making ion-substitution reactions easier.<sup>[31]</sup> Generally, the relatively high temperature and pressure promote the kinetic energy of chemical reaction and ion mobility, hence facilitating the dissolution of solid phase Co ions and confinement of various Cu ions from the solution into the Co solid lattice. It can be proposed that the solid phase Co ions are thermodynamically less stable than the liquid phase Cu ions under hydrothermal conditions, accelerating the diffusion of Cu ions in the solution and the release of Co ions. This improves the ionic exchange reaction via a cation substitution. Owing to larger surface-to-volume ratios, the diffusion rates may be higher. The reaction barrier for nucleation can be reduced because of low coordination facets (high-energy sites for nucleation). The efficient dissolution of the template Co MOF under hydrothermal conditions at the solid-liquid interface allows for a subsequent replacement by Cu ions from the solution. The etching action of OH<sup>-</sup> species adsorbed on the surface of Co MOF can break the metal-ligand Co-DHTA coordination and direct the dissociation of Co<sup>2+</sup> from the DHTA. Side-by-side, under hydrothermal conditions, it is easier for Cu<sup>2+</sup> ions to leave a hydration shell and participate in the cation substitution reaction with Co ions. The robust solvation of outgoing Co ions and fast diffusion of guest Cu ions favor the progress of a desired cation exchange at the interface. Consequently, the released Co<sup>2+</sup> and diffused Cu<sup>2+</sup> metal centers bond with the OH<sup>-</sup> at the interface, establishing the

binary hydroxide Cu/Co junction due to a significant balance in diffusion rates between host Co ions and guest Cu ions. Subsequently, the ultrafine La(OH)<sub>3</sub> layer was electrochemically immobilized on the binary hydroxide Cu/Co junction, acquiring a binder-free ternary hydroxide La@Cu/Co core-shell composite on the NF skeleton.



The selection of Cu and Co metal ions for the MOF-derived binary hydroxide Cu/Co junction is based on their low cost, large abundance, and variable oxidation states. Alongside this, the presence of La can influence both the conductivity and redox-capability of the resulting hybrid.<sup>[32-34]</sup> Furthermore, the coexistence of Co(OH)<sub>2</sub>, Cu(OH)<sub>2</sub>, and La(OH)<sub>3</sub> species in a core-shell heterostructure induces the Faradaic redox processes of CoOOH/CoO<sub>2</sub>, CuOH/Cu<sub>2</sub>O, and LaO(OH)<sub>3</sub> couples, respectively, during charging-discharging. The CoOOH, CuOH, and LaO(OH)<sub>3</sub> as the redox-active and a conductive wrapping layer for electroactive components are anticipated to be propitious for quick electron transfer during Faradaic redox reactions.<sup>[34]</sup> The as-synthesized La@Cu/Co/NF core-shell electrode can be directly served as the working electrode without additional treatment, averting the impact of agents or binders on electrochemical activity.

To monitor the textural properties of as-prepared Co MOF, binary hydroxide Cu/Co junction, and ternary hydroxide La@Cu/Co core-shell composite, FE-SEM and TEM characterizations were executed. As shown in Figure S1a-b, Co MOF micron-sized rods with smooth surfaces and hexagonal sections were successfully developed. After the cation exchange reaction, the binary hydroxide Cu/Co junction with spatial nanogranule self-assembled microrods-like structure was formed. The vertically grown nanogranules layer is fluffy and porous with a dense amount of Cu/Co microstructures (Figure S1c-d). This observation suggests that the OH<sup>-</sup> can diffuse inward to direct the cation exchange reaction between the Co-DHTA and Cu<sup>2+</sup> ions during the growth/etching process, enabling the transformation

of interiors to Cu/Co microstructures. The diffused  $\text{Cu}^{2+}$  ions into the interior of the template Co MOF can break the Co–DHTA coordination bonds and react with Co ions, elaborating the structural transformation from the Co MOF framework to form the binary hydroxide Cu/Co junction. Figure 2a–b illustrates the typical SEM images of the La@Cu/Co core-shell composite. After an electrolytic deposition process, plenty of tiny  $\text{La(OH)}_3$  nano-ornamentation is uniformly attached to the complexed Cu/Co junction. Meanwhile, both microstructural binary hydroxide Cu/Co core and outer interlaced ornamentation generate more electrolyte-accessible area, thereby facilitating rapid  $\text{OH}^-$  diffusion.

Figure 2c–d and Figure S2a–b depict the TEM micrographs of the La@Cu/Co hybrid, where one can observe a core-shell architecture with the binary hydroxide Cu/Co microrods core surrounded by a porous layer. This corresponds with the SEM images. The heterogeneous microtubular arrays consist of nanogranule self-assembled microrods that are arranged into 1D vertically aligned architectures, meanwhile, the porous  $\text{La(OH)}_3$  layer wraps the microtubular arrays. It goes without saying that the distinctive architecture can promote the active materials' utilization efficiency, aid in the electron transport process, and strengthen electrochemical properties. The corresponding TEM-EDS mapping results of a heterostructural La@Cu/Co core-shell hybrid (Figure 2e) elucidate the uniform distribution of Co, O, Cu, and La elements, verifying the conversion of the template Co MOF into the binary hydroxide Cu/Co junction. Moreover, the composition of the binder-free La@Cu/Co/NF core-shell electrode was investigated by the ICP–Ms characterization. Findings elucidate the Co, Cu, and La content as 19.7, 16.8, and 3.8%, respectively throughout the configured electrode.

The XRD signals of binder-free Co MOF/NF, binary hydroxide Cu/Co/NF, and ternary hydroxide La@Cu/Co/NF electrodes were

analyzed to examine their crystal configurations as shown in Figure 3a. The sharp intense diffraction peaks at ca.  $44.4^\circ$ ,  $51.8^\circ$ , and  $76.4^\circ$  in all three samples are mainly attributed to the (1 1 1), (2 0 0), and (2 2 0) facets, respectively, of metallic Ni (JCPDS No. 04–0850) and ascribed to the NF substrate.<sup>[33]</sup> The XRD spectra of Cu/Co/NF and La@Cu/Co/NF electrodes illustrate the  $2\theta$  signatures at  $25.8^\circ$  and  $50.4^\circ$  which are consistent with the (3 0 –4) and (1 0 2) crystal facets of  $\text{Co(OH)}_2$  (JCPDS No. 48–0091 and JCPDS No. 45–0031),<sup>[35,36]</sup> respectively. Besides, the diffraction peaks located at  $\sim 36^\circ$ ,  $43^\circ$  and  $74.1^\circ$  are attributed to (1 1 1), (1 3 1), and (2 4 0) planes of  $\text{Cu(OH)}_2$  (JCPDS No. 35–0505), respectively.<sup>[37]</sup> Furthermore, for the core-shell La@Cu/Co composite, the supplementary peak located at around  $28.1^\circ$  can be accredited to the (1 0 1) plane of  $\text{La(OH)}_3$ , consistent with the standard card (JCPDS No. 36–1481).<sup>[38]</sup> The chemical configuration, surface valence states, and bonding of ternary hydroxide La@Cu/Co core-shell heterostructure were studied by XPS characterization as illustrated in Figure 3. The typical XPS survey spectrum in Figure 3b witnesses the existence of Co, Cu, La, O, and C (induced by contaminants and investigated as a reference for calibration) components, corroborating the successful  $\text{Co}^{2+}$ – $\text{Cu}^{2+}$  ion exchange and decoration of  $\text{La(OH)}_3$  film. The Gaussian fitting method was applied to fit the collected data and further understand the surface chemistry of components in the La@Cu/Co core-shell composite. The high-resolution XPS spectrum of the Co 2p core level is represented in Figure 3c. It can be observed that the Co 2p region features two spin-orbit bands of  $\text{Co } 2\text{p}_{3/2}$  and  $\text{Co } 2\text{p}_{1/2}$  with two shake-up satellite signatures, certifying the prominence of  $\text{Co}^{2+}$ / $\text{Co}^{3+}$  multiple electroactive sites. These electrochemical species favor surface-dependent redox reactions and thereby a high electrochemical performance can be anticipated. The  $\text{Co}^{3+}$  characteristic peaks for the low energy band  $\text{Co } 2\text{p}_{3/2}$  and high energy band  $\text{Co } 2\text{p}_{1/2}$  are located at 778.2 and 795.6 eV, while the  $\text{Co}^{2+}$

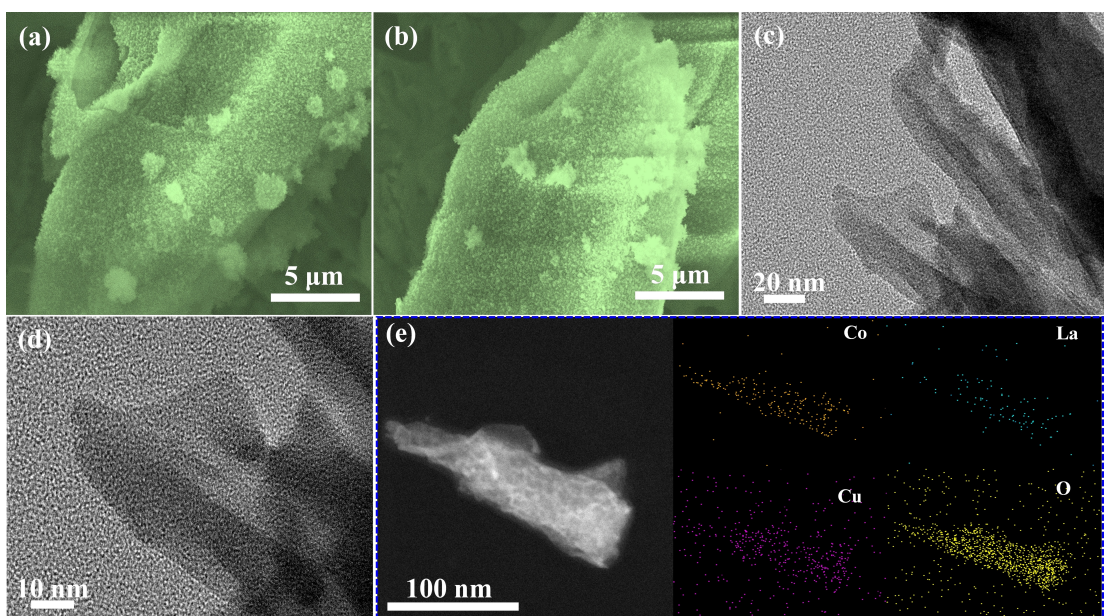


**Figure 2.** Morphological features of a heterostructural La@Cu/Co core-shell composite. (a–b) SEM and (c–d) TEM images. (e) Bright-field TEM image and corresponding EDS elemental maps of Co, O, Cu, and La elements.

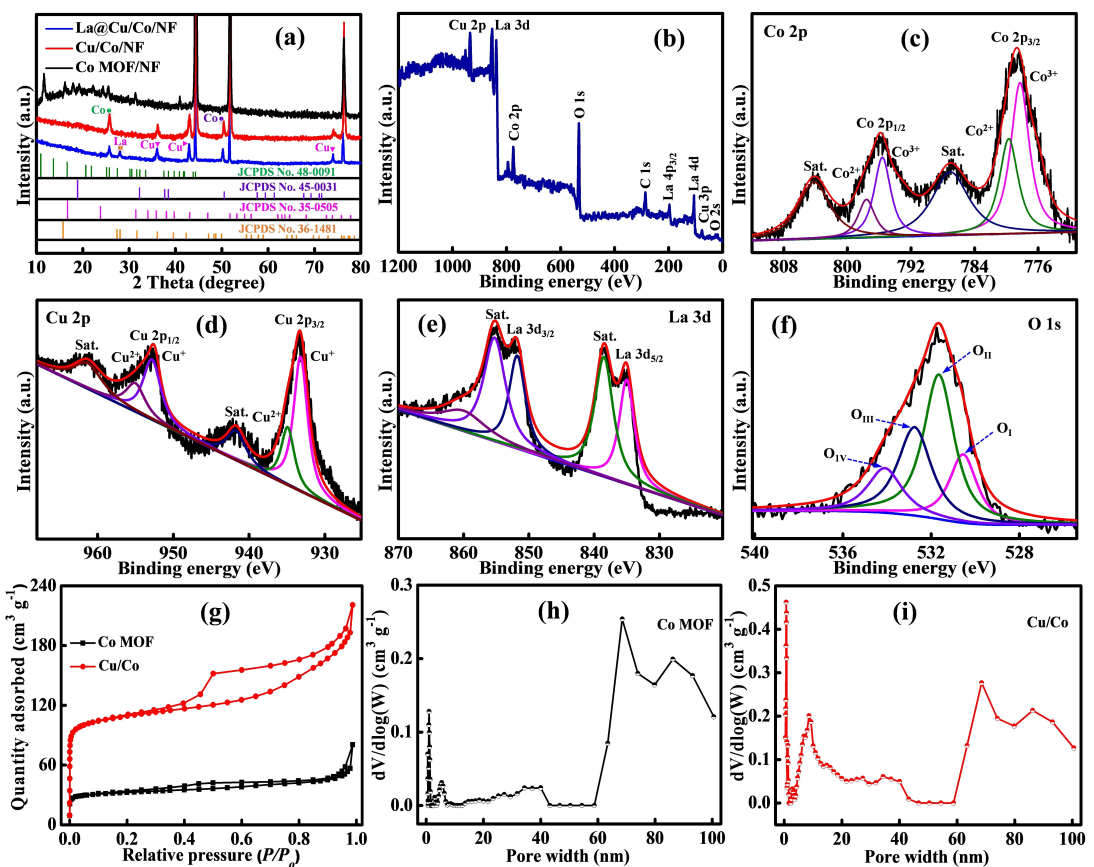


**Figure 3.** (a) XRD patterns of the as-prepared samples. Material characterization of La@Cu/Co core-shell electrode. (b) XPS survey spectrum and high-resolution XPS scan of (c) Co 2p, (d) Cu 2p, (e) La 3d, and (f) O 1s. (g)  $N_2$  adsorption/desorption isotherms and corresponding pore size distribution profiles of (h) Co MOF and (i) Cu/Co junction.

peaks of Co 2p<sub>3/2</sub> and Co 2p<sub>1/2</sub> can be found at 779.7 and 797.6, respectively. Side-by-side, the satellites (identified as "Sat") at the binding energies of ~787.1 and 804.2 eV refer to the Co<sup>2+</sup> state.<sup>[39]</sup>

Similarly, the high-resolution Cu 2p XPS signal displays two spin-orbit doubles corresponding to Cu 2p<sub>3/2</sub> and Cu 2p<sub>1/2</sub> components accompanied by two satellites (Figure 3d). The Gaussian deconvolution of these major bands presents fitted peaks at 933.2 and 952.8 eV, ascribing to Cu<sup>+</sup> sites caused by Cu(OH) or Cu<sub>2</sub>O. On the other hand, the peaks at 934.9 and 955.1 eV ensure the presence of Cu<sup>2+</sup> (Cu(OH)<sub>2</sub>). The trace amount of possible Cu(OH) or Cu<sub>2</sub>O may be beyond the detection standard of the XRD system. The satellite peaks at 941.8 and 961.5 eV are assigned to the paramagnetic characteristics of the Cu<sup>2+</sup> chemical state.<sup>[34]</sup> The formal oxidation valence state of La<sup>3+</sup> in the La 3d core level can be deconvoluted into two signatures at 835 and 851.8 eV, which indicate the spin-orbital interactions of La 3d<sub>5/2</sub> and La 3d<sub>3/2</sub>, respectively (Figure 3e). Additionally, the corresponding satellite peaks of La 3d<sub>5/2</sub> and La 3d<sub>3/2</sub> bands are detected around ~838.5 and 855.3 eV, respectively.<sup>[40]</sup> As illustrated in Figure 3f, the O 1s XPS spectrum can be fitted with four distinct oxygen contributions associated with La–O bonds (O<sub>I</sub>, ~530.6 eV), Co–O/Cu–O (O<sub>II</sub>, 531.7 eV), metal–OH "Co–OH/Cu–OH/La–OH" (O<sub>III</sub>, 532.7 eV), and OH groups "H–O–H" (O<sub>IV</sub>, 534.1 eV).<sup>[41]</sup> The O<sub>II</sub>/O<sub>III</sub> metal–O peaks

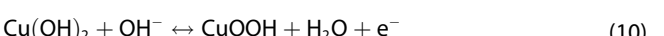
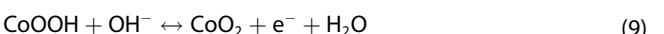
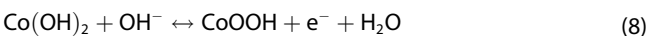
and O<sub>III</sub> metal–O peaks theoretically originate from the metal–oxygen interaction and bound hydroxide groups, respectively. Meanwhile, the O<sub>IV</sub> peak signifies the adsorbed H<sub>2</sub>O.<sup>[39]</sup> The role of La<sup>3+</sup> centers in the energy storage performance of hybrid electrodes can be realized via its involvement in Faradaic redox reactions, conductivity fine-tuning, and structure stabilization. These characteristics present the La<sup>3+</sup> sites as valuable components for exploring novel electrode materials. Briefly, the La<sup>3+</sup> centers can serve as an electron acceptor during electrochemical redox reactions, accelerating the electron transfer processes between reactive species, and tuning the electronic configuration.<sup>[42]</sup> The capability of La(OH)<sub>3</sub> to establish certain oxidation states and experience robust Faradaic redox reactions can positively impact the reaction kinetics and charge storage efficiency. It can stabilize the hybrid structure, thereby retaining the performance during charging-discharging cycles. Overall, incorporating La<sup>3+</sup> centers reinforces the electric conductivity, which is crucial for promoting the rate capability. Besides, La<sup>3+</sup> in conjunction with Cu/Co ions generates synergistic effects, boosting the electrochemical performance by manipulating the redox reactivity.<sup>[43]</sup>

To reveal the specific surface area and structural porosities of samples, the BET analyses were performed. Figure 3g shows the obtained  $N_2$  adsorption-desorption profiles of template Co MOF and binary hydroxide Cu/Co junction (the residue powder

in both solvothermal and hydrothermal reactions was utilized). The samples reveal typical type IV isotherms with prominent H<sub>3</sub> hysteresis loops in the relative pressure range of  $0.2 \leq P/P_0 \leq 0.96$ , manifesting the existence of rich mesopores.<sup>[44]</sup> The relatively large gas adsorption capability within the low-pressure range ( $P/P_0 < 0.2$ ) validates the presence of some micropores. Whereas, the improved N<sub>2</sub> adsorption behavior at a pressure range of  $0.96 \leq P/P_0 \leq 1$  proposes the generation of macropores. Thanks to abundant mesopores and micropores created by the template MOF framework, Co MOF and Cu/Co samples reach the BET surface area and total pore volume of  $123.64 \text{ m}^2 \text{ g}^{-1}/0.12 \text{ cm}^3 \text{ g}^{-1}$  and  $419.2 \text{ m}^2 \text{ g}^{-1}/0.34 \text{ cm}^3 \text{ g}^{-1}$ , respectively. This suggests that the cationic exchange reaction can efficiently increase the specific surface area of the materials, which may be credited to lattice distortion and defects induced by Cu insertion and additional growth as well as recrystallization processes under hydrothermal conditions.<sup>[45]</sup> The corresponding pore size distributions of samples are illustrated in Figure 3h and Figure 3i. The Co MOF and Cu/Co samples elucidate similar micropore/mesopore/macropore-dominant structure with a median pore width of 15.04 and 3.94 nm, respectively. The large specific surface area and favorable pore architecture expose more electrochemical reactive sites. The tunable porosities not only promote the ion diffusion kinetics but also strengthen the energy storage behavior.

The electrochemical properties of as-designed Co MOF/NF, binary hydroxide Cu/Co/NF, and ternary hydroxide La@Cu/Co/NF electrodes were subsequently evaluated by CV and GCD analyses utilizing a three-electrode cell system. The CV results of these electrodes at  $10 \text{ mVs}^{-1}$  scan rate are presented in Figure 4a. Apparently, all samples exhibit distinct redox peaks, demonstrating their favorable faradaic redox reaction behaviors. The independent redox signatures resemble the transient reactions, which occur simultaneously between Co<sup>2+</sup>/Co<sup>3+</sup>/

Co<sup>4+</sup>, Cu<sup>2+</sup>/Cu<sup>+</sup>, and La<sup>3+</sup>/La<sup>4+</sup> redox conversion chemistry (Equations (8–12)).<sup>[32–34,46,47]</sup>



Apparently, the heterostructural La@Cu/Co core-shell electrode realizes a higher current signal and larger CV integral area in comparison with those of other electrodes. Such a finding suggests that the core-shell composite electrode can store more energy, which originates from its hierarchical architecture and synergism between ternary metal centers. Incorporating a rare earth element with a binary metal hydroxide junction can enhance the electronic structure of the resultant electrode and increase the number of electrochemically active species. Figure 4b depicts the comparative GCD profiles of electrodes at a fixed discharge current density of  $1 \text{ A g}^{-1}$  in the working potential range of 0–0.55 V vs. Hg/HgO. Evidently, the La@Cu/Co/NF core-shell electrode displays a marked extension in the discharge time, approaching the larger specific capacitance. This illustrates that the core-shell heterostructure comprising the La(OH)<sub>3</sub> nano-integration and the binary hydroxide Cu/Co junction reinforces the electrochemical response and offers more oxidation states. Within the electrode configuration, the nonlinearity of GCD plots further elucidates the predominant redox processes with a pseudocapacitive-type charge storage behavior.

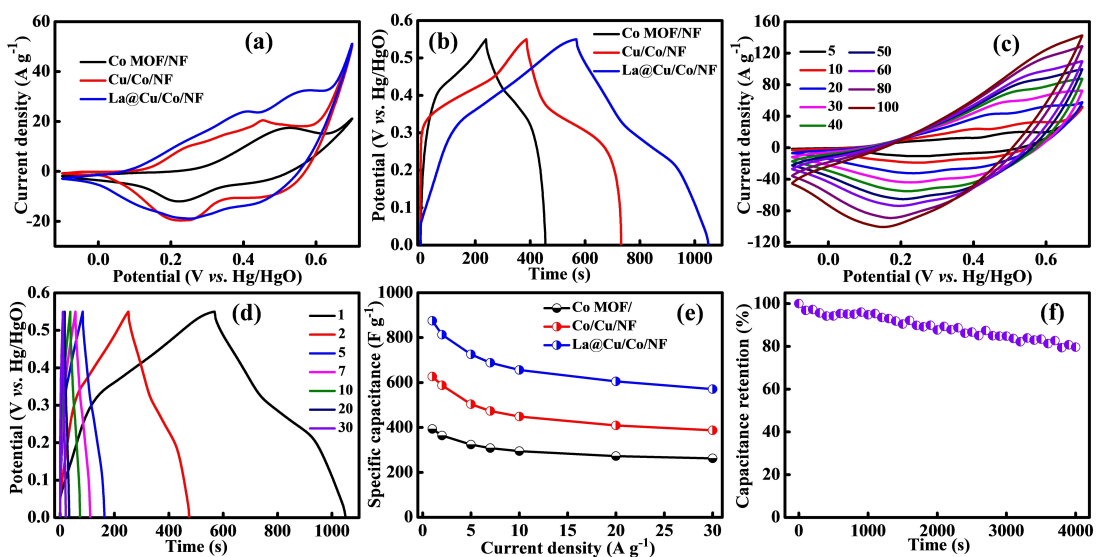


**Figure 4.** Electrochemical performance of MOF-derived electrodes. (a) CV patterns of electrodes at  $10 \text{ mVs}^{-1}$  and (b) GCD plots of electrodes at  $1 \text{ A g}^{-1}$ . (c) CV curves at different scanning rates and (d) GCD spectra at different discharge current densities of La@Cu/Co/NF core-shell electrode. (e) Specific capacitance of different electrodes as a function of current density. (f) Cyclic stability performance of La@Cu/Co/NF electrode at a high current density of  $20 \text{ A g}^{-1}$ .

To study the electrochemical dynamics of electrodes, the CV analysis of Co MOF/NF, Cu/Co/NF, and La@Cu/Co/NF at varying sweep rates is represented in Figure 4c and Figure S3a–b. Upon increasing the scan rate, the redox peaks can be observed, the CV shape is similar and related to each other. The enhanced current signals demonstrate smaller internal and charge transfer resistances with strong redox reaction processes along exposed surfaces. The redox peaks of the Co MOF/NF electrode gradually disappear at higher scan rates due to polarization.

The performance of the La@Cu/Co/NF core-shell electrode in terms of reaction kinetics was studied in depth. The linear relationship between the peak current ( $I_p$ ) and the square root of the scanning rate yields the values of  $R^2$ , which are 0.998 and 0.996, ratifying that the current response stems from a diffusion-dominated process (Figure S3c). This finding elucidates that the diffusion of OH<sup>-</sup> ions is a rate-determining step during the redox reaction. As can be seen, the linearity of the plot illustrates that the charge transfer process within the La(OH)<sub>3</sub>@Cu/Co core-shell electrode arises from the involvement of a surface-controlled process (capacitive process) and diffusion-controlled process (Faradaic reaction). To corroborate the penetration of ions along the electrode during the electrochemical process, the diffusion coefficient (D) can be expressed by the Randles–Sevcik equation as follows:<sup>[33,48]</sup>

$$I_p = 2.69 \times 10^5 \times A \times C \times n^{0.5} \times D^{0.5} \times \vartheta^{0.5} \quad (13)$$

where  $I_p$ ,  $\vartheta$ ,  $A$ ,  $C$ , and  $n$  are the peak current derived from the CV signal, applied scan rate, electrode surface area, electrolyte concentration, and number of electrons transferred, respectively. The D-value of the anodic and cathodic scan can reach  $2.17 \times 10^{-3}$  and  $1.79 \times 10^{-3} \text{ cm}^2 \text{s}^{-1}$ , respectively. These values imply that the as-synthesized La@Cu/Co heterostructure can supply effective diffusion sites for boosting the ion diffusion process rate.

To verify the mechanism of the charge storage by the La@Cu/Co/NF electrode during the electrochemical process, the logarithmic correlation between the peak current response and scan rate is profoundly explored by the Power law (Equation (14)), where  $a$  and  $b$  are adjustable coefficients:<sup>[47]</sup>

$$I_p = a\vartheta^b \quad (14)$$

The collected CV plots can be employed to observe the redox features of the electrode active material via the linear dependence plot (Figure S3d). The  $b$  value evaluates the electrochemical behavior and can be derived from the slope of the linear fit for log(peak current) versus log(scan rate). Theoretically, the representative electrochemical reaction can be a surface-controlled (capacitive) process if the  $b$  value reaches 1, whereas the contribution mostly belongs to the diffusion-controlled (battery type) redox process when the value of the  $b$  value is 0.5. The La@Cu/Co/NF core-shell electrode presents the  $b$  values of 0.666 and 0.756 for the anodic and cathodic peak current response, respectively, manifesting that the electrochemical kinetics and the charge retention mechanism are dominated by both battery-like and capacitive behaviors.

To analyze the dominating charge transfer kinetics and quantitatively identify the capacitive and diffusion contributions at various scanning rates, the respective capacitive-controlled ( $k_1\vartheta$ ) and diffusion-controlled ( $k_2\vartheta^{1/2}$ ) modes are estimated based on the following formula:

$$i(V) = K_1 \times \vartheta + K_2 \times \vartheta^{0.5} \quad (15)$$

where  $V$  reflects the voltage,  $\vartheta$  is the sweep rate, and  $K_1$  and  $K_2$  are parameters that influence the capacitance and diffusion control. The integral pink area demonstrates the percentage of the surface capacitance, which yields about 24.4, ~33, and ~24% of the overall reaction process over Co-MOF/NF, Cu/Co/NF, and La@Cu/Co/NF electrodes, respectively, at  $10 \text{ mVs}^{-1}$  (Figure 5a–c). The percentages of diffusion and surface capacitance control in the total reaction process of Co MOF/NF, Cu/Co/NF, and La@Cu/Co/NF electrodes at different scanning rates are depicted in Figure 5d–f. Upon increasing the applied sweep rate, the capacitive contribution progressively enhances, revealing an effective surface charge storage behavior. The proportion of the diffusion control contribution of Co MOF/NF, Cu/Co/NF, and La@Cu/Co/NF electrodes decreases from 82.6%–26%, 75.7%–28.3%, and 82.5%–41.3% as the scan speed increases from  $5\text{--}100 \text{ mVs}^{-1}$ , respectively.

What's more, the GCD spectra of electrodes were systematically assessed under diverse current densities from  $1\text{--}30 \text{ Ag}^{-1}$  in an electrochemical window spanning  $0\text{--}0.55 \text{ V}$  relative to Hg/HgO as illustrated in Figure 4d and Figure S3e–f. Both charge and discharge segments reveal well-defined voltage plateaus, corresponding to the observed redox characteristics of the CV results. This manifests that the constructed electrodes store charge via Faradaic reaction processes as anticipated for a pseudocapacitive system. The improved symmetry elucidates reversible redox reactions caused by modified kinetics of OH<sup>-</sup> migration and diffusion and robust mass transport at the electrolyte/electrode interface. The calculated specific capacitance of Co MOF/NF, Cu/Co/NF, and La@Cu/Co/NF reaches 393.3, 627, and  $874.8 \text{ Fg}^{-1}$ , respectively, at  $1 \text{ Ag}^{-1}$  (Figure 4e). Notably, the capacitance retention rate of these electrodes at  $1\text{--}30 \text{ Ag}^{-1}$  realizes 66.7, 61.8, and 65.2%, respectively. At a lower current density of  $1 \text{ Ag}^{-1}$ , the diffusion time is sufficient for electrolyte ion permeation into heterointerfaces, which accounts for a higher capacitance at  $1 \text{ Ag}^{-1}$ . Conversely, the swift kinetic feature under higher current densities weakens the prompt permeation of electrolyte ions along the electrode, leading to rapid decay in the capacitance value.

The diffusion kinetics and interfacial charge transportation of electrodes could be investigated by the EIS technique in the frequency range of  $0.1 \text{ Hz}\text{--}100 \text{ kHz}$  at the open circuit potential with a signal amplitude of 5 mV. Figure S4 elucidates the Nyquist plots of Co MOF/NF, Cu/Co/NF, and La@Cu/Co/NF electrodes, displaying a half-circle arc within the high-frequency realm (reflects the charge transfer resistance " $R_{ct}$ "), followed by an inclined line in the low-frequency realm (symbolizes the Warburg or diffusion resistance " $Z_w$ "). The equivalent series resistance ( $R_s$ ) can be represented by the intercept of the semicircle arc with the real axis ( $Z'$ ). The  $R_s$  of Co MOF/NF, Cu/Co/NF, and La@Cu/Co/NF electrodes are  $0.05\text{--}0.1 \text{ }\Omega$ ,  $0.1\text{--}0.2 \text{ }\Omega$ , and  $0.05\text{--}0.1 \text{ }\Omega$ , respectively, at  $100 \text{ kHz}$ .

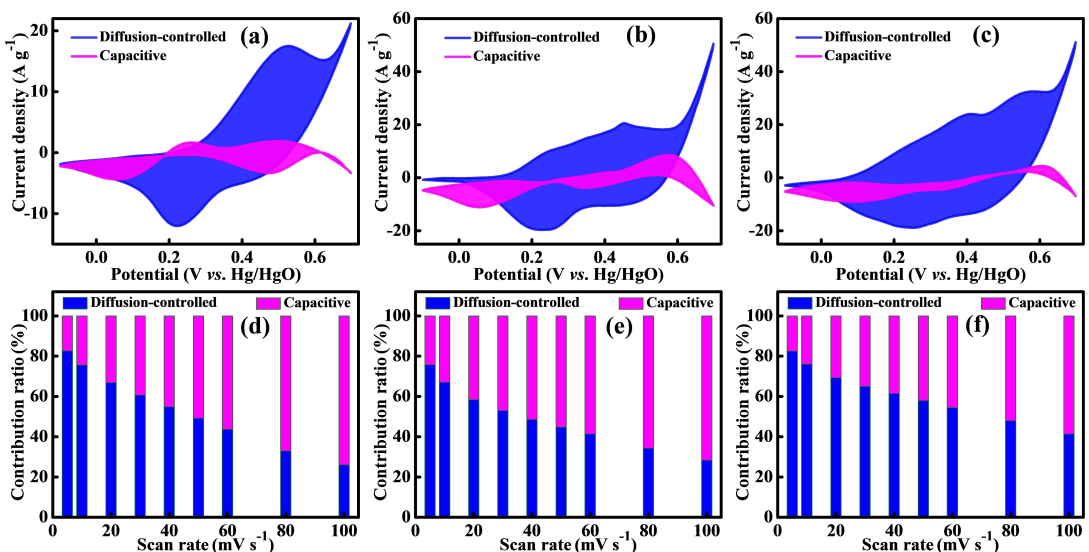


**Figure 5.** Contributions of surface-controlled (pink) at 10 mVs<sup>-1</sup> of (a) Co MOF/NF, (b) Cu/Co/NF, and (c) La@Cu/Co/NF electrodes. Capacitive (pink) and diffusive (blue) contributions at various scanning rates of (d) Co MOF/NF, (e) Cu/Co/NF, and (f) La@Cu/Co/NF electrodes.

Co/NF, and La@Cu/Co/NF reach a small value of 0.82, 0.87, and 0.89 Ω, respectively, signifying satisfactory electrolyte interaction with the accessible electroactive sites, low contact and solution resistances.<sup>[49]</sup> Among all, the La@Cu/Co core-shell electrode exhibits the smallest semicircle diameter (2.72 Ω), manifesting enhanced electric conductivity of electrode material and modulated electron transfer redox kinetics. The  $R_{ct}$  is observed to be 4.63 and 3.42 Ω for Co MOF/NF and Cu/Co/NF, respectively. The minimal  $R_{ct}$  value and Warburg slope of a heterostructural La@Cu/Co/NF electrode confirm the conductivity and ionic diffusion, enabling efficient charge storage capacity.<sup>[50]</sup> Given this, the electron transmission rate in the La@Cu/Co core-shell composite is faster, thereby hastening the charging and discharging rate, which can be verified by the related morphology (Figure S5).

Thus, the core-shell architecture promotes intrinsic reactivity, surpassing the capacitance of individual components. Overall, the CV and GCD studies prove the superiority of a heterostructural La@Cu/Co/NF core-shell electrode over pristine Co MOF/NF and binary hydroxide Cu/Co/NF. The improved capacitance retention of the La@Cu/Co/NF electrode corresponds to the structural, compositional, and chemical synergy articulations within the electrode's active material. In particular, the high surface energy due to electrochemical active sites like oxidative Co, Cu, and La metal centers and porous nano-granules ornamentation can decrease the charge transfer resistance and equivalent series resistance as well. The La(OH)<sub>3</sub> shell layer in a heterostructural La@Cu/Co core-shell composite can improve Faradaic redox reactions by supplying an additional set of reactive sites for redox reactions, hindering the deactivation of active sites during the electrochemical cycling, accelerating the electron transportation to the core during redox reactions, and allowing ions to penetrate to the core. Besides, in using a heterostructural La@Cu/Co core-shell composite, both core and shell can participate in Faradaic

reactions and the La(OH)<sub>3</sub> shell provides multi-site activity. This induces a core-shell synergy. The co-presence of multiple active constituents with distinct redox potentials enhances the charge storage activity. Moreover, heterointerfaces can create strong electronic interactions, hasten electron transportation rates, and enlarge the electrode-electrolyte contact area. Hence optimizing the utilization efficiency of active constituents, ensuring intensified redox capability throughout the entire reaction process, and consequently strengthening the electrochemical behavior. Furthermore, the cyclic stability performance of a heterostructural La@Cu/Co/NF core-shell electrode was monitored for 4000 GCD cycles at a higher current density of 20 A g<sup>-1</sup> and the corresponding capacitance retention as a function of the cycle number is demonstrated in Figure 4f. It is clearly seen that the capacitance retention of the electrode can sustain up to 79.6% after 4000 cycles, confirming the compositional and chemical optimization within the complexed core-shell composite for the long-term sustainability of continuous charge-discharge processes. The La(OH)<sub>3</sub> shell may serve as a barrier to protect the binary hydroxide Cu/Co core from direct exposure to the electrolyte, thereby yielding a high utilization efficiency of the electrode material. It affords mechanical strength to the Cu/Co junction, maintaining the structural integrity of the core during electrochemical cycling and volume change associated with the ion insertion/extraction. As observed, the specific capacitance value of the proposed La@Cu/Co/NF core-shell electrode is highly encouraging compared with the recently presented electrodes-based LDHs (Table S1).

The employability for practical applications was investigated by assembling a two-electrode hybrid device in a 3 M KOH aqueous electrolyte solution. The La@Cu/Co/NF core-shell electrode was chosen as the cathode, meanwhile, the AC/NF served as the anode. Based on the charge balance principle (Equation (3)), the mass loading ratio of the anode to the cathode was estimated as 4.3:1, with respective masses of ~5.3

and 1.23 mg, respectively. Electrochemical properties and energy storage characteristics of the AC/NF anode were measured with a conventional three-electrode system (see the Supplementary Information for details). Both CV and GCD tests of the AC/NF anode present a typical electric double-layer capacitance (EDLC) behavior, making the commercially available AC appropriate for serving as a negative electrode material for an ASC system (Figure S6). The operational potential window of the AC/NF anode spans from 0–1 V vs. Hg/HgO with electrochemical surface reactions-assisted EDLC mechanism, while that of the La@Cu/Co/NF cathode ranges from -0.1–0.7 V vs. Hg/HgO with well-developed redox characteristics and pseudocapacitive-type behavior of charge storage. Such a distinction underscores the rationale behind establishing an aqueous ASC system with the La@Cu/Co/NF cathode and AC/NF anode. Therefore, achieving an extended total operational potential window for the resulting device. The CV measurements of as-fabricated La@Cu/Co/NF//AC aqueous ASC configuration were explored with varying operational potentials at 50 mVs<sup>-1</sup> as shown in Figure 6a. The assembled system shows a negligible polarization phenomenon in the potential window of 0–1.6 V, implying good electrochemical stability. On the other hand, a sudden increase in the current response can be detected at the tail of the CV profile when the working voltage range is set at 1.7 V, signifying the occurrence of an oxygen evolution reaction.

Figure 6b depicts the representative CV curves of the La@Cu/Co/NF//AC ASC device within the voltage window of 0–1.6 V at several sweep rates from 5–100 mVs<sup>-1</sup>. The deviation from an ideal rectangular CV shape of the EDLC is mainly ascribed to the occurrence of robust Faradaic redox reaction processes. As stated earlier, the cathode works based on a pseudocapacitive-like energy storage mechanism, whereas the anode has an EDLC-like behavior. The complementary contributions of both cathode and anode materials play crucial in

boosting the electrochemical performance of a supercapacitor cell because each electrode has a diverse charge storage mechanism. For instance, the electrochemical double-layer charge storage behavior of the anode and pseudocapacitance of the cathode allows for enhanced charge-discharge characteristics. The complementary properties of the cathode and anode materials (e.g., specific surface area, porosities, conductivity, and stability) promote the energy and power outcomes. Pairing transition metal hydroxides and carbon optimize the overall charge storage performance and Long-term cyclability. The tunable ionic transport of commercial amorphous AC with tunable electronic conductivity ensures a more efficient charge transfer process and robust durability. This synergy reinforces the overall charge-discharge rate and cyclic stability. Thus, the reasonable match between the pseudocapacitive La@Cu/Co/NF and capacitive AC/NF induces the complementary contribution of both Faradic and non-Faradic reactions at interfaces, which can be verified by the CV results. Evidently, the minor shape change of CV signals even at higher scanning rates elucidates the enhanced reversibility and rate capability of the device. As the voltage range broadens to 1.6 V, the GCD curve at a current density of 1 Ag<sup>-1</sup> reveals overcharging with a widened voltage window up to 1.6 V. Such a critical issue may lead to severe electrode degradation and reduce the device's lifespan.<sup>[51]</sup> Accordingly, the device's optimal working voltage range stands at 0–1.55 V to yield higher Coulombic efficiency and regulated pseudocapacitive performance. The GCD curves of the device in the optimal voltage range of 0–1.55 V at various current densities are presented in Figure 6c. The nonlinear charge-discharge graphs indicate the Faradaic charge storage characteristics of the device. Conspicuously, the good symmetry of GCD curves ensures boosted charge transfer kinetics and modulated reversibility of the charge-discharge process. The improved pseudocapacitive performance and excellent Coulombic efficiency can be inferred from the analyzed GCD results.

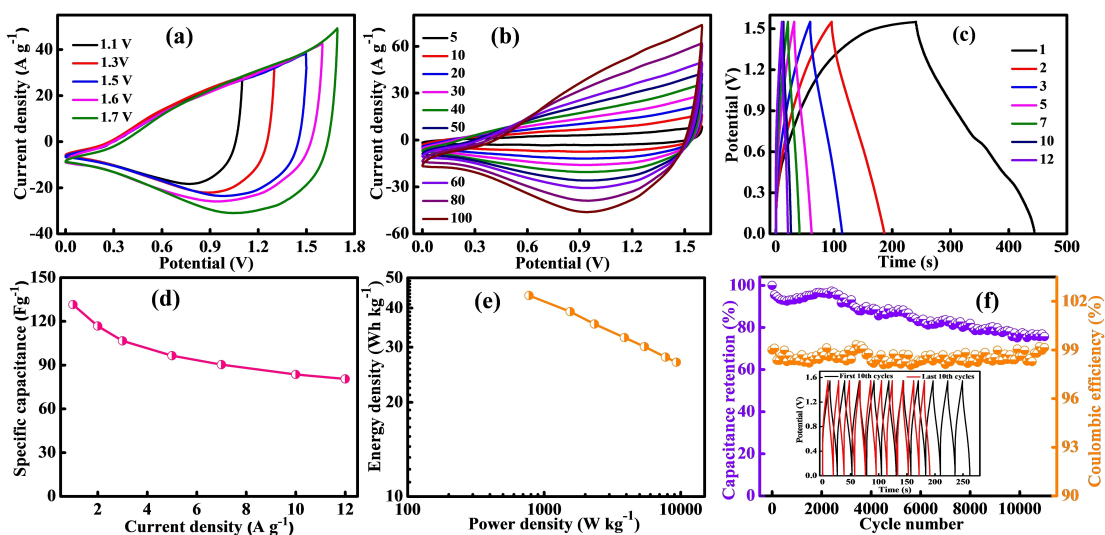


**Figure 6.** Energy storage capability of the sandwiched La@Cu/Co/NF//AC ASC device. (a) CV tests in different working potentials at 50 mVs<sup>-1</sup>, (b) CV curves at different scanning rates, (c) GCD data at different current densities, (d) relationship between specific capacitance and current density, (e) Ragone plot, and (f) capacitance retention and Coulombic efficiency of the device over 11,000 GCD cycles at 10 Ag<sup>-1</sup>. Inset-f depicts the first and last 10<sup>th</sup> cycles of the cyclic stability test.

The device's specific capacitance can be computed based on the discharge time as listed in Figure 6d. Accordingly, the configured La@Cu/Co/NF//AC ASC system obtains a high specific capacitance of  $131.5 \text{ F g}^{-1}$  at  $1 \text{ A g}^{-1}$  and sustains 61.2% after approaching a large current density of  $12 \text{ A g}^{-1}$ , revealing a high capability retention. Considering the total mass of cathode and anode materials, the integrated device acquires a specific energy density of  $43.9 \text{ Wh kg}^{-1}$  to a particular power of  $775 \text{ W kg}^{-1}$ . Besides, the device still provides  $\sim 39$ , 35.6, 32.2, 30.1, 27.9, and  $26.9 \text{ Wh kg}^{-1}$  at 1551, 2335.9, 3873.1, 5426.4, 7748.8, and  $9307.1 \text{ W kg}^{-1}$ , respectively (Figure 6e). A detailed comparison of the La@Cu/Co/NF//AC device and other previously reported supercapacitor configurations is represented in Table S2. Obviously, the charge storage capability of the La@Cu/Co/NF//AC device outperforms some recently reported systems employing hydroxide or MOF-based cathodes such as Ni/Co hydroxides ( $42.4 \text{ Wh kg}^{-1}$  at  $823.2 \text{ W kg}^{-1}$ ),<sup>[52]</sup> Ni<sub>2</sub>O<sub>3</sub>@Ni-MOF ( $32.6 \text{ Wh kg}^{-1}$  at  $348.9 \text{ W kg}^{-1}$ ),<sup>[53]</sup> Ni-MOF@Co(OH)<sub>2</sub> ( $45.7 \text{ Wh kg}^{-1}$  at  $1400 \text{ W kg}^{-1}$ ),<sup>[54]</sup> Co(OH)<sub>2</sub> ( $28.5 \text{ Wh kg}^{-1}$  at  $1500 \text{ W kg}^{-1}$ ),<sup>[55]</sup> CoMn-LDH ( $5.9 \text{ Wh kg}^{-1}$  at  $250 \text{ W kg}^{-1}$ ),<sup>[56]</sup> CBC-N@LDH composite ( $36.3 \text{ Wh kg}^{-1}$  at  $800.2 \text{ W kg}^{-1}$ ),<sup>[57]</sup> CoAl-LDH ( $55.04 \text{ Wh kg}^{-1}$  at  $387.9 \text{ W kg}^{-1}$ ),<sup>[58]</sup> and CNHC-12 h ( $41.8 \text{ Wh kg}^{-1}$  at  $800 \text{ W kg}^{-1}$ ).<sup>[59]</sup> Additionally, even after 11,000 charge-discharge cycles at  $10 \text{ A g}^{-1}$ , the device still sustains a retention rate of 76.4% with a remarkable Coulombic efficiency of  $\sim 98.3\%$  after undergoing 11,000 cycles as discerned in Figure 6f. As displayed, the device experiences a three-stage energy storage process mode involving narrow capacitance degradation with the first 400 cycles, activation and capacitance-enhancing step in the range of 600–~2000 cycles, and gradual decline stage. The progressive enhancement in the capacitance retention with the period of 600–~2000 cycles is mainly attributed to the reinforcement of charge-discharge redox reactions induced by electrolyte infiltration and self-activation dynamics.<sup>[60,61]</sup> The ion activation and structural adaptive arrangement during charge/discharge processes may supply new electrochemical reactive sites. The unique porous architecture of MOF-derived compounds can strengthen the redox-reactive sites, hence, yield a high pseudocapacitive capability. The floppy connection between electroactive centers and electrolyte ions as well as the sufficient activation of integrated substances promote the capacitance retention.<sup>[62]</sup> The inset-f showcases the first and last 10<sup>th</sup> GCD cycles of the cyclic stability test, presenting evidence for the enhanced long-term lifespan.

### 3. Conclusions

In summary, we employed a dual approach of heterointerfacing and structural engineering to achieve the *in situ* direct growth of the La@Cu/Co core-shell composite on the NF skeleton through a simple solvothermal method-cation exchange reaction-electrodeposition technique. The special compositional and structural features allow a convenient path for the transmission of electrons and modify the OH<sup>-</sup>—embedding/separation in electrochemical processes. The strong synergy among

reactive constituents affords numerous active sites for electrochemical Faradaic reactions. Consequently, the heterostructural La@Cu/Co/NF core-shell cathode displays an enhanced pseudocapacitive performance by simultaneously exhibiting  $874.8 \text{ F g}^{-1}$  at  $1 \text{ A g}^{-1}$  and reaching a satisfactory rate performance with capacitance retention of ca. 65.2% even at a high current density of  $30 \text{ A g}^{-1}$ . The capacitance of surface capacitive and diffusion-driven contributions can be controllably tuned by interface regulation, realizing a high electrochemical performance of the electrode. Assembling into an ASC configuration, it accomplishes an operational voltage range of 1.55 V, attains a high energy of  $43.9 \text{ Wh kg}^{-1}$  at a power of  $775 \text{ W kg}^{-1}$ , and sustains 76.4% after 11,000 cycles. The inherent binder-free engineering and reinforced redox processes boost the electrochemical efficiency of a heterostructural La@Cu/Co core-shell composite through synergistic effects. The proposed work therefore underscores a potential contender to optimize the performance of MOF-derived multicomponent compounds via a heterointerfacing and structural engineering pathway.

### Author Contributions

Diab Khalafallah: Methodology, Visualization, Formal analysis, Writing—original draft, Writing – review & editing, Investigation, Conceptualization, Validation. Yunxiang Zhang: Validation, Formal analysis, Data curation. Qinfang Zhang: Writing – review & editing, Investigation, Supervision, Validation.

### Funding

This work is supported by the National Natural Science Foundation of China (No. 12474276 and 12274361), the Natural Science Foundation of Jiangsu Province (BK20211361), and the College Natural Science Research Project of Jiangsu Province (20KJA430004).

### Conflict of Interests

The authors declare no conflict of interest.

### Data Availability Statement

The data that support the findings of this study are available from the corresponding author upon reasonable request.

**Keywords:** MOF • Binary hydroxide Cu(OH)<sub>2</sub>/Co(OH)<sub>2</sub> junction • La(OH)<sub>3</sub> • Core-shell heterostructures • Binder-free electrodes • Supercapacitors

- [1] D. Khalafallah, F. Qiao, C. Liu, J. Wang, Y. Zhang, J. Wang, Q. Zhang, P. H. L. Notten, *Coord. Chem. Rev.* **2023**, *496*, 215405.
- [2] D. Khalafallah, Y. Zhang, H. Wang, J.-M. Lee, Q. Zhang, *Chin. J. Catal.* **2023**, *55*, 44–115.

- [3] J. Zhao, M. Zhou, J. Chen, L. Wang, Q. Zhang, S. Zhong, H. Xie, Y. Li, *Small* **2023**, *19*, 2303353.
- [4] W. Liu, X. Zhang, Y. Xu, L. Wang, Z. Li, C. Li, K. Wang, X. Sun, Y. An, Z. Wu, Y. Ma, *Adv. Funct. Mater.* **2022**, *32*, 2202342.
- [5] H. Yu, D. Chen, X. Ni, P. Qing, C. Yan, W. Wei, J. Ma, X. Ji, Y. Chen, L. Chen, *Energy Environ. Sci.* **2023**, *16*, 2684.
- [6] J. Zhou, S. Zhang, Y. Zhou, W. Tang, J. Yang, C. Peng, Z. Guo, *Electrochem. Energy Rev.* **2021**, *4*, 219.
- [7] Q. Lu, D. Li, B. Zi, Q. Lu, M. Chen, J. Zhang, Z. Zhu, Q. Liu, *ACS Energy Lett.* **2022**, *7*, 4204.
- [8] C. Zhong, Y. Deng, W. Hu, J. Qiao, L. Zhang, J. Zhang, *Chem. Soc. Rev.* **2015**, *44*, 7484–539.
- [9] V. Augustyn, P. Simon, B. Dunn, *Energy Environ. Sci.* **2014**, *7*, 1597–1614.
- [10] L. Lin, W. Lei, S. Zhang, Y. Liu, G. G. Wallace, J. Chen, *Energy Storage Mater.* **2019**, *19*, 408–423.
- [11] R. Liu, A. Zhou, X. Zhang, J. Mu, H. Che, Y. Wang, T.-T. Wang, Z. Zhang, Z. Kou, *Chem. Eng. J.* **2021**, *412*, 128611.
- [12] J. Sun, L. Guo, X. Sun, J. Zhang, L. Hou, L. Li, S. Yang, C. Yuan, *Batteries Supercaps* **2019**, *2*, 820–841.
- [13] H. W. Park, K. C. Roh, *J. Power Sources* **2023**, *557*, 232558.
- [14] K.-B. Wang, Q. Xun, Q. Zhang, *EnergyChem* **2020**, *2*, 100025.
- [15] X. Li, X. Yang, H. Xue, H. Pang, Q. Xu, *EnergyChem* **2020**, *2*, 100027.
- [16] S. Sahoo, R. Kumar, E. Joanni, R. K. Singh, J.-J. Shim, *J. Mater. Chem. A* **2022**, *10*, 13190–13240.
- [17] J. Yan, T. Liu, X. Liu, Y. Yan, Y. Huang, *Coord. Chem. Rev.* **2022**, *452*, 214300.
- [18] I. Hussain, S. Iqbal, C. Lamiel, A. Alfantazi, K. Zhang, *J. Mater. Chem. A* **2022**, *10*, 4475–4488.
- [19] Q. Dong, M. Li, M. Sun, F. Si, Q. Gao, X. Cai, Y. Xu, T. Yuan, S. Zhang, F. Peng, Y. Fang, S. Yang, *Small Methods* **2021**, *5*, 2100878.
- [20] Y. Wang, W. Xie, D. Li, P. Han, L. Shi, Y. Luo, G. Cong, C. Li, J. Yu, C. Zhu, J. Xu, *Sci. Bull.* **2020**, *65*, 1460–1469.
- [21] L. Han, J. Luo, R. Zhang, W. Gong, L. Chen, F. Liu, Y. Ling, Y. Dong, Z. Yong, Y. Zhang, L. Wei, X. Zhang, Q. Zhang, Q. Li, *ACS Nano* **2022**, *16*, 14951–14962.
- [22] R. Manikandan, C. J. Raj, A. D. Savariraj, P. Thondaiman, W.-J. Cho, H.-M. Jang, B. C. Kim, *Electrochim. Acta* **2021**, *393*, 139060.
- [23] D. Khalafallah, Y. Zhang, Q. Zhang, *FlatChem* **2024**, *43*, 100602.
- [24] N. Swain, B. Saravanakumar, M. Kundu, L. Schmidt-Mende, A. Ramadoss, *J. Mater. Chem. A* **2021**, *9*, 25286–25324.
- [25] L. M. Da Silva, R. Cesár, C. M. R. Moreira, J. H. M. Santos, L. G. De Souza, B. M. Pires, R. Vicentini, W. Nunes, H. Zanin, *Energy Storage Mater.* **2020**, *27*, 555–590.
- [26] F. Zeng, X. Song, J. Liang, X. Zhang, X. Sha, X. Wu, H. Zhou, Z. Liu, W. Wu, C. Jiang, *J. Mater. Chem. A* **2022**, *10*, 25148–25158.
- [27] Z. Wu, L. Li, J.-M. Yan, X.-B. Zhang, *Adv. Sci.* **2017**, *4*, 1600382.
- [28] G. A. Drake, L. P. Keating, M. Shim, *Chem. Rev.* **2023**, *123*, 3761–3789.
- [29] B. J. Beberwyck, Y. Surendranath, A. P. Alivisatos, *J. Phys. Chem. C* **2013**, *117*, 19759–19770.
- [30] M. C. Rath, *Handbook on Synthesis Strategies for Advanced Materials: Vol.1: Techniques and Fundamentals* (Eds: A. K. Tyagi, R. S. Ningthoujam), Springer, Singapore **2021**, pp. 623–656, <https://doi.org/10.1007/978-981-16-1807-9>.
- [31] L. Li, X. Lv, L. Jin, K. Du, J. Jiang, X. Zhao, H. Liang, Y. Guo, X. Wang, *Appl. Catal. B: Environ.* **2024**, *344*, 123586.
- [32] Z. Wang, S. Lu, W. Xu, Z. Wang, H. Zuo, *New J. Chem.* **2022**, *46*, 7202–7211.
- [33] D. Khalafallah, Q. Zhang, *J. Energy Storage* **2024**, *95*, 112621.
- [34] L. Kumar, P. K. Boruah, S. Borthakur, L. Saikia, M. R. Das, S. Deka, *ACS Appl. Nano Mater.* **2021**, *4*, 5250–5262.
- [35] Y. Cai, Y. Ye, S. Wu, J. Liu, C. Liang, *RSC Adv.* **2016**, *6*, 78219–78224.
- [36] K. Li, B. Zhao, J. Bai, H. Ma, Z. Fang, X. Zhu, Y. Sun, *Small* **2020**, *16*, 2001974.
- [37] W. Al Zoubi, D. K. Yoon, Y. G. Kim, Y. G. Ko, *J. Colloid Interface Sci.* **2020**, *573*, 31–44.
- [38] G. Xin, Y. Zhai, Y. Xing, W. Sun, J. Liu, W. Hu, J. Song, C. Bunlin, B. Zhang, X. Liu, *J. Alloys Compd.* **2023**, *945*, 169345.
- [39] Y. Chen, J. Yang, H. Yu, J. Zeng, G. Li, B. Chang, C. Wu, X. Guo, G. Chen, L. Zheng, X. Wang, *ACS Appl. Energy Mater.* **2022**, *5*, 6772–6782.
- [40] T. Vijayaraghavan, R. Sivasubramanian, S. Hussain, A. Ashok, *ChemistrySelect* **2017**, *2*, 5570–5577.
- [41] D. K. Yadav, J. Muhammed, S. Deka, *ACS Appl. Nano Mater.* **2023**, *6*, 13513–13523.
- [42] H. Peng, J. Liang, R. Zhao, F. Wang, G. Wei, J. Zhou, G. Ma, Z. Lei, *Electrochim. Acta* **2019**, *300*, 290–298.
- [43] A. Shameem, P. Devendran, A. Murugan, V. Siva, S. A. Bahadur, *J. Energy Storage* **2023**, *73*, 108856.
- [44] F. Zhang, Z. Zhao, L. Ai, H. Li, S. Zhang, X. Wang, J. Qiu, *ACS Appl. Energy Mater.* **2024**, *7*, 5839–5847.
- [45] T. Li, Y. Hu, J. Zhang, H. Li, K. Fang, J. Wang, Z. Wang, M. Xu, B. Zhao, *Nano Energy* **2024**, *126*, 109690.
- [46] S. N. Kanimozihi, A. K. Putiyaveettil, B. Natesan, A. Al Souwaleh, J. J. Wu, G. Landi, A. Sambandam, *ACS Appl. Electron. Mater.* **2024**, *6*, 918–930.
- [47] J. Li, S. Li, Y. Huang, Z. Liu, C. Chen, Q. Ding, H. Xie, Y. Xu, S. Sun, H. Li, *ACS Appl. Mater. Interfaces* **2024**, *16*, 6998–7013.
- [48] S. Fleischmann, J. B. Mitchell, R. Wang, C. Zhan, D. E. Jiang, V. Presser, V. Augustyn, *Chem. Rev.* **2020**, *120*, 6738–6782.
- [49] S. Ghosh, H. R. Inta, M. Chakraborty, G. Tudu, H. V. S. R. M. Koppiasetti, K. S. Paliwal, D. Saha, V. Mahalingam, *ACS Appl. Nano Mater.* **2022**, *5*, 7246–7258.
- [50] D. S. Abraham, M. Vinoba, M. Bhagiyalakshmi, *ACS Appl. Nano Mater.* **2024**, *7*, 5791–5801.
- [51] J. Zhang, M. Gu, X. Chen, *Micro Nano Eng.* **2023**, *21*, 100229.
- [52] L. Ye, L. Zhao, H. Zhang, B. Zhang, H. Wang, *J. Mater. Chem. A* **2016**, *4*, 9160–9168.
- [53] G. Li, H. R. Cai, X. L. Li, J. Zhang, D. S. Zhang, Y. F. Yang, J. Xiong, *ACS Appl. Mater. Interfaces* **2019**, *11*, 37675–37684.
- [54] X. Y. Shi, T. Deng, G. S. Zhu, *J. Colloid Interf. Sci.* **2021**, *593*, 214–221.
- [55] T. Deng, Y. Lu, W. Zhang, M. L. Sui, X. Y. Shi, D. Wang, W. T. Zheng, *Adv. Energy Mater.* **2018**, *8*, 1702294.
- [56] A. D. Jagadale, G. Guan, X. Li, X. Du, X. Ma, X. Hao, A. Abudula, *J. Power Sources* **2016**, *306*, 526–534.
- [57] F. Lai, Y. E. Miao, L. Zuo, H. Lu, Y. Huang, T. Liu, *Small* **2016**, *12*, 3235–3244.
- [58] Z. Gao, C. Bumgardner, N. Song, Y. Zhang, J. Li, X. Li, *Nat. Commun.* **2016**, *7*, 11586.
- [59] X. Jia, Y. Zhao, X. Xu, Z. Xiao, S. Lv, F. Zhou, Q. Zhang, C. Chen, J. Liu, L. Wang, *ACS Appl. Energy Mater.* **2023**, *6*, 9108–9117.
- [60] J. Lee, T. S. Lim, S. G. Jo, S. Jeong, H.-J. Paik, I. W. Ock, S. Lee, K. J. Yu, J. W. Lee, *Chem. Eng. J.* **2023**, *476*, 146515.
- [61] R. Chen, X. He, Y. Liu, W. Xu, T. T. Nguyen, L. Cheng, *J. Energy Storage* **2024**, *91*, 111965.
- [62] W. Zheng, J. Halim, L. Yang, H. O. Badr, Z. M. Sun, P. O. Persson, J. Rosen, M. W. Barsoum, *Batteries Supercaps* **2022**, *5*, e202200151.

Manuscript received: July 21, 2024

Revised manuscript received: October 18, 2024

Accepted manuscript online: November 1, 2024

Version of record online: November 20, 2024